Supplemental Information for "Rigidity control of general origami structures"

Rongxuan Li[1] and Gary P. T. Choi[1]

[1] *Department of Mathematics, The Chinese University of Hong Kong, Hong Kong, China*

Supplementary Note 1. THE GEOMETRY OF DIFFERENT ORIGAMI STRUCTURES

In the main text, we provided one representative view of all types of origami structures studied in this work. Fig. S1 shows additional views of each type of origami structure to help readers better understand their geometry and structure.

Also, it is noteworthy that the calculation of the infinitesimal rigidity matrix A depends on the vertex coordinates of the origami structure. As discussed in [1, 2], changes in geometric parameters (i.e., the folding percentage) of the Miura-ori do not affect the rigidity percolation behavior. It is natural to ask whether the geometric parameters of other origami structures influence their rigidity percolation behavior.

To address this, we present in Fig. S2(a) the simulation results for the Huffman Rectangular Weave origami structure with 129 facets, a folding percentage of 25%, and $k = 1, 2, 4, 8, 16, 32$ under both selection rules. We then increase the folding percentage to 50% and 75% while keeping the configuration and resolution unchanged, and the corresponding simulation results (100 simulations for each k) are shown in Fig. S2(b)–(c). As shown on the left of Fig. S2, the geometries with 50% and 75% folding percentages differ significantly from the 25% case considered in the main text. Nevertheless, the 3×4 plots on the right demonstrate that, under both the Most Efficient and Least Efficient selection rules, the simulation results for the evolution of the normalized DOF and rigidity percolation remain highly consistent. In particular, the trend of the normalized DOF evolution and the increasing sharpness in the transition of the probability P of obtaining a minimum-DOF structure are similar across different folding percentages and rules as k increases. A comparable trend is also observed in Fig. S3 for the Huffman Waterbombs structure with different folding percentages (25%, 50%, and 75%), confirming the robustness of the rigidity percolation behavior across different geometric configurations. Therefore, we conclude that the DOF evolution and explosive rigidity percolation transition are independent of the geometry of the general origami structure.

Besides, in the main text, we stated a theorem regarding the number of sub-planarity constraints required to control the planarity of an n-sided polygonal facet. Below, we give the detailed proof of the theorem.

Theorem. *The number of sub-planarity constraints required to control the planarity of an n-sided polygonal facet is exactly $n - 3$.*

Proof. We first show that the edge and no-shear constraints contribute a rank of $n + (n - 3) = 2n - 3$ to the rigidity matrix.

Note that the first triangle $(\mathbf{v}_1, \mathbf{v}_2, \mathbf{v}_3)$ in the triangulation of the n-sided polygonal facet contributes three edge constraints. These constraints are linearly independent and form a $3 \times 3n$ submatrix with nonzero entries only at columns corresponding to $\mathbf{v}_1, \mathbf{v}_2, \mathbf{v}_3$. Each subsequent triangle $(\mathbf{v}_k, \mathbf{v}_i, \mathbf{v}_j)$ introduces two new edge constraints, which again contribute two independent rows to the rigidity matrix due to their sparsity pattern (i.e., non-overlapping support in the matrix rows). These rows involve only the coordinates of $\mathbf{v}_k$, $\mathbf{v}_i$, and $\mathbf{v}_j$. There are $(n - 3)$ such additional triangles beyond the first one, contributing $2(n - 3)$ additional rows. Therefore, the edge and no-shear constraints together contribute a total rank of

$$3 + 2(n - 3) = 2n - 3. \tag{S1}$$

Since the polygon has n vertices in $\mathbb{R}^3$, it has in total $3n$ degrees of freedom. Subtracting 6 for the rigid body motions (3 translations and 3 rotations), the maximal rank attainable is $3n - 6$. Thus, the minimum number of constraints needed to reach full rank is

$$3n - 6 - (2n - 3) = n - 3. \tag{S2}$$

Hence, we conclude that the above $(n - 3)$ planarity constraints are necessary to control the planarity of the polygonal facet.

Moreover, note that it suffices to enforce planarity between each adjacent pair of triangles in the triangulation. Since each new triangle shares an edge with the previous one, enforcing planarity along these $n - 3$ internal edges is sufficient to ensure the entire polygon remains planar. Therefore, we conclude that the $n - 3$ planarity constraints in the above argument constitute one of the minimal sets required to control the polygonal facet. Therefore, no constraint is redundant.

□

Proposition Supplementary Note 1.1 (Triangulation-induced length constraints do not restrict infinitesimal bending)**.** *Let a polygonal facet have vertices* $\{x_i\}_{i=1}^n \subset \mathbb{R}^3$ *that are coplanar in a plane* Π *with unit normal* n*. Let* $\mathcal{E}_{\text{int}}$ *be the set of internal edges of* any *valid triangulation of this facet (e.g.,* $|\mathcal{E}_{\text{int}}| = n-3$*), and impose the corresponding no-shear (internal edge-length) constraints*

$$g_{ij}(x) := \|x_i - x_j\|^2 - \ell_{ij}^2 = 0, \qquad (i,j) \in \mathcal{E}_{\text{int}}.$$

Let $J_{\text{int}}(x)$ *denote the rigidity matrix obtained by linearizing these constraints at* x*. Then every purely out-of-plane infinitesimal motion of the form*

$$\dot{x}_i = w_i\, n, \qquad i = 1, \dots, n,$$

with arbitrary scalars $w_1, \dots, w_n \in \mathbb{R}$*, satisfies*

$$J_{\text{int}}(x)\, \dot{x} = 0.$$

In particular, triangulation-induced internal edge-length constraints are first-order insensitive to out-of-plane infinitesimal motions at a flat configuration and therefore do not control infinitesimal out-of-plane bending of the facet.

Proof. For any $(i,j) \in \mathcal{E}_{\text{int}}$, linearizing $g_{ij}(x) = 0$ yields

$$Dg_{ij}(x) \cdot \dot{x} \;=\; 2(x_i - x_j) \cdot (\dot{x}_i - \dot{x}_j) = 0.$$

Since $x_i, x_j \in \Pi$, the edge vector $(x_i - x_j)$ lies in Π and is orthogonal to the plane normal n, i.e., $(x_i - x_j) \cdot n = 0$. Taking $\dot{x}_i = w_i n$ gives

$$(x_i - x_j) \cdot (\dot{x}_i - \dot{x}_j) = (x_i - x_j) \cdot \big((w_i - w_j)n\big) = (w_i - w_j)\,(x_i - x_j) \cdot n = 0,$$

so every such out-of-plane infinitesimal motion satisfies the linearized internal edge-length constraints. □

Supplementary Note 2. NUMERICAL ERROR ANALYSIS FOR DEGREES OF FREEDOM COMPUTATION

In our simulations, the degrees of freedom (DOF) is computed from the numerical rank of the rigidity matrix $A \in \mathbb{R}^{m \times n}$. Specifically, the DOF is obtained by

$$\text{DOF} \;=\; 3V - \text{rank}(A) - 6. \tag{S3}$$

We compute the rank via a QR-based criterion. Let $A(:, q)$ denote a column-reordered matrix, where q=`colamd(A, size(A))`, and let

$$R = \text{qr}\big(A(:,q), 0\big).$$

We use an adaptive tolerance

$$\tau \;=\; \max(m,n) \cdot \epsilon \cdot |R_{11}|, \tag{S4}$$

where ϵ is machine precision (double precision in MATLAB). A diagonal thresholding rule estimates the numerical rank by counting the number of diagonal (pivot) entries of the triangular factor R whose magnitudes exceed a tolerance τ, i.e., $\hat{r} \;=\; \#\{\, i \;:\; |R_{ii}| \geq \tau \,\}$. This is consistent with standard numerical linear algebra practice, as the rank is not an exact integer-valued quantity in floating-point arithmetic, and its stability depends on the separation between significant singular values and numerical noise.

To verify that the reported DOF trajectories are not artifacts of numerical rank decisions, we perform a tolerance-sweep robustness check. Specifically, we perturb the baseline tolerance in Eq. (S4) by several orders of magnitude,

$$\tau_k = 10^k \tau, \qquad k \in \{-K, \dots, K\},$$

and recompute the DOF for each τ_k. We find that the DOF trajectories remain unchanged over a wide range of tolerance multipliers for most densities ρ. When discrepancies occur, they are confined to a narrow neighborhood of the rigidity transition, where the constraint matrix becomes more ill-conditioned and numerical rank determination

is expected to be most sensitive. Importantly, in all cases, the qualitative trends and the observed phase-transition behavior remain unchanged. The tolerance-sweep results are summarized in Fig. S4.

From Fig. S4, we observe that the DOF trajectories are highly stable with respect to the tolerance multiplier. For the Hex/Tri instance, a minor discrepancy of +1 DOF appears only when the tolerance multiplier is in the range 10^4–10^5, and only after approximately step 40. In contrast, for the asymmetric origami instance, the unnormalized DOF remains unchanged across all tested tolerance multipliers. Overall, these results confirm that our reported DOF trajectories are robust to numerical rank tolerance choices, and the main conclusions of the paper are not affected by numerical rank artifacts.

Supplementary Note 3. THE DEGREES OF FREEDOM (DOF) IN THE ORIGAMI STRUCTURES WITH DIFFERENT PATTERN RESOLUTIONS

In the main text, we presented the rigidity percolation results for one size of each origami pattern. Here, we extend our analysis by considering multiple resolutions for each type of origami structure.

Specifically, for the class of Periodic Origami structures (Fig. S5(a)), in addition to the Miura-Ori with 400 facets shown in the main text, we include views of the Miura-Ori with 100 and 225 facets. For the Huffman Rectangular Weave, we include structures with 129, 313, and 577 facets. For the Huffman Waterbombs, we show structures with 178, 403, and 718 facets. For the class of Rotational Origami structures (Fig. S5(b)), we show the Lang Oval with 69, 103, and 137 facets; the Hex/Tri with 97, 205, and 1285 facets; and the Lang Honeycomb with 91, 367, and 829 facets. For the class of Perforated Origami structures (Fig. S5(c)), we show Kirigami Honeycomb with 72, 120, and 276 facets; Perforated Triangle with 39, 106, and 342 facets; and Auxetic Triangle with 88, 206, and 570 facets.

For all types of origami structures at different resolutions, we perform numerical simulations using the same setup as described in the main text. We compute the normalized DOF and the probability P of obtaining a minimum-DOF structure at each planarity constraint density ρ. We further present our observations on the normalized DOF and the transition width across different resolutions and values of k. While some variations on the same structure across the different resolutions may exist, the overall DOF evolution trend for each structure remains consistent with the corresponding observations presented in the main text. The results provided here may serve as a reference for readers interested in specific structures and may help guide further studies on the rigidity control of particular origami designs, especially in identifying the optimal k to achieve a prescribed low transition width.

We first recall the definition of the transition width. The transition width is defined as the interval of ρ over which the probability P increases from 0 to 1. More precisely, it is given by

$$\rho_w = \rho_1 - \rho^0, \tag{S5}$$

where ρ_1 is the minimum ρ for which $P = 1$, and ρ^0 is the maximum ρ for which $P = 0$ in our simulations.

For the DOF evolution under the Most Efficient selection rule of the periodic origami and rotational origami structures (see Fig. S6 and Fig. S7), increasing the resolution reduces the proportion of facets needed to reach the final DOF. For the DOF evolution of perforated origami structures (see Fig. S8), increasing the resolution does not affect the proportion of facets needed to reach the final DOF. In all of the above-mentioned origami structures, while the normalized DOF decreases as the resolution increases, the final DOF remains unchanged. The overall trend of DOF evolution with increasing k is consistent across all resolutions. Specifically, as k increases, the DOF in individual simulations tends to drop more rapidly in the early stages, eventually exhibiting a sharp and consistent linear decline across simulations until reaching the final DOF.

For the transition width under the Most Efficient selection rule of periodic origami structures, increasing k from small values (e.g., $k = 1, 2$) leads to a slight increase of transition width of the probability P from 0 to 1, while further increasing k results in a sharper transition width (see Fig. S9). This behavior is consistent with observations in the Miura-ori structure. More explanations and quantitative analyses are provided in [1]. Additionally, the transition width generally remains the same across different resolutions for most values of k. For rotational origami structures, increasing k from 1 generally results in a sharper transition of the probability P from 0 to 1, especially for structures with higher resolution (see Fig. S10). The transition width tends to decrease with resolution for most values of k. For perforated origami structures, increasing k from small values (e.g., $k = 1, 2$) leads to a slight increase of the transition width of the probability P from 0 to 1, while further increasing k results in a sharper transition width (see Fig. S11). The transition width generally remains the same across different resolutions for most values of k.

For the DOF evolution under the Least Efficient selection rule across general origami structures (see Fig. S12, Fig. S13, and Fig. S14), the selection rule does not affect the underlying structure of the origami. Similar to the Most Efficient selection rule, while the normalized DOF decreases with increasing resolution, the final DOF remains unchanged. The overall trend of DOF evolution with increasing k is consistent across all resolutions. Specifically, as k increases, the DOF in individual simulations tends to remain flat for as long as possible, especially when triangular

facets constitute a larger proportion of the structure, and then inevitably experience a linear decline. If the structure converges to a single-DOF configuration, a nonlinear region may appear after the linear regime due to redundancy in the facet planarity constraints left. In contrast, structures with multiple final DOFs are more likely to be reached through a consistent linear decline.

For the transition width under the Least Efficient selection rule in periodic origami structures, increasing k from 1 to 2 leads to a significantly sharper transition (see Fig. S15). The transition width generally remains unchanged across different resolutions for most values of k. For rotational origami structures, the relation between the transition width and k follows a similar trend to the periodic structures. Increasing the resolution results in a slight increase in the transition width for the Lang Honeycomb structure, but a decrease for Lang Oval and Hex/Tri (see Fig. S16). For perforated origami structures, increasing k from 1 also sharpens the transition, although most of these structures already exhibit a sharp transition even at $k = 1$ (see Fig. S17). Due to this initial sharpness and the nature of DOF decay under the Least Efficient selection rule, the transition width remains nearly 0 across different resolutions for most values of k.

Supplementary Note 4. THE CRITICAL TRANSITION DENSITY FOR DIFFERENT ORIGAMI STRUCTURES

In the main text, we presented a 3D plot of the critical transition density ρ^* for nine types of origami structures, each with three configurations, with triangular facet ratio information provided. Here, we provide the corresponding numerical ρ^* values in Table S1, Table S2, and Table S3. Also, in the main text, we fit the simulated ρ^* using a tanh-based model:

$$\rho^*_{\text{fit}} = a \cdot \tanh\left(b \cdot (-1)^r \cdot \log(k) + c\right) + dt + f. \tag{S6}$$

For each of the nine types of origami structures, we consider the simulation results for different parameters $(-1)^r \log(k) \in \{-\log 32, -\log 16, -\log 8, -\log 4, -\log 2, 0, \log 2, \log 4, \log 8, \log 16, \log 32\}$ at three different resolutions, which gives $11 \times 3 = 33$ data points. We then formulate the curve fitting problem as a constrained optimization problem and use the `fmincon` solver in MATLAB to search for the best-fit parameters a, b, c, d, f with $0 \le \rho^*_{\text{fit}} \le 1$ based on the 33 data points. The visualization of the simulated and fitted results is shown in Fig. S18. To evaluate the fitting accuracy, we consider the Root Mean Squared Error (RMSE) and Normalized RMSE as follows:

$$\text{RMSE} = \sqrt{\frac{1}{n}\sum_{i=1}^{n}\left(\rho^*_{\text{fit}_i} - \rho^*_i\right)^2}, \tag{S7}$$

$$\text{Normalized RMSE} = \frac{\sqrt{\frac{1}{n}\sum_{i=1}^{n}\left(\rho^*_{\text{fit}_i} - \rho^*_i\right)^2}}{\max_{\{1\le i\le n\}}(\rho^*_i) - \min_{\{1\le i\le n\}}(\rho^*_i)}, \tag{S8}$$

where $n = 33$ is the total number of data points used in the fitting of one origami structure, ρ^*_i is the simulated critical transition density of the i-th structure (with $i = 1, 2, \ldots, n$), and $\rho^*_{\text{fit}_i}$ is the corresponding fitted result. For each origami structure, the fitted parameters along with the corresponding RMSE and normalized RMSE are provided in Table S4. For all origami structures, the low RMSE and normalized RMSE values indicate that the fitted models can effectively match the simulation results.

SUPPLEMENTARY REFERENCES

[1] R. Li and G. P. T. Choi, Proc. R. Soc. A **481**, 20240826 (2025).
[2] S. Chen and L. Mahadevan, Proc. Natl. Acad. Sci. **116**, 8119 (2019).

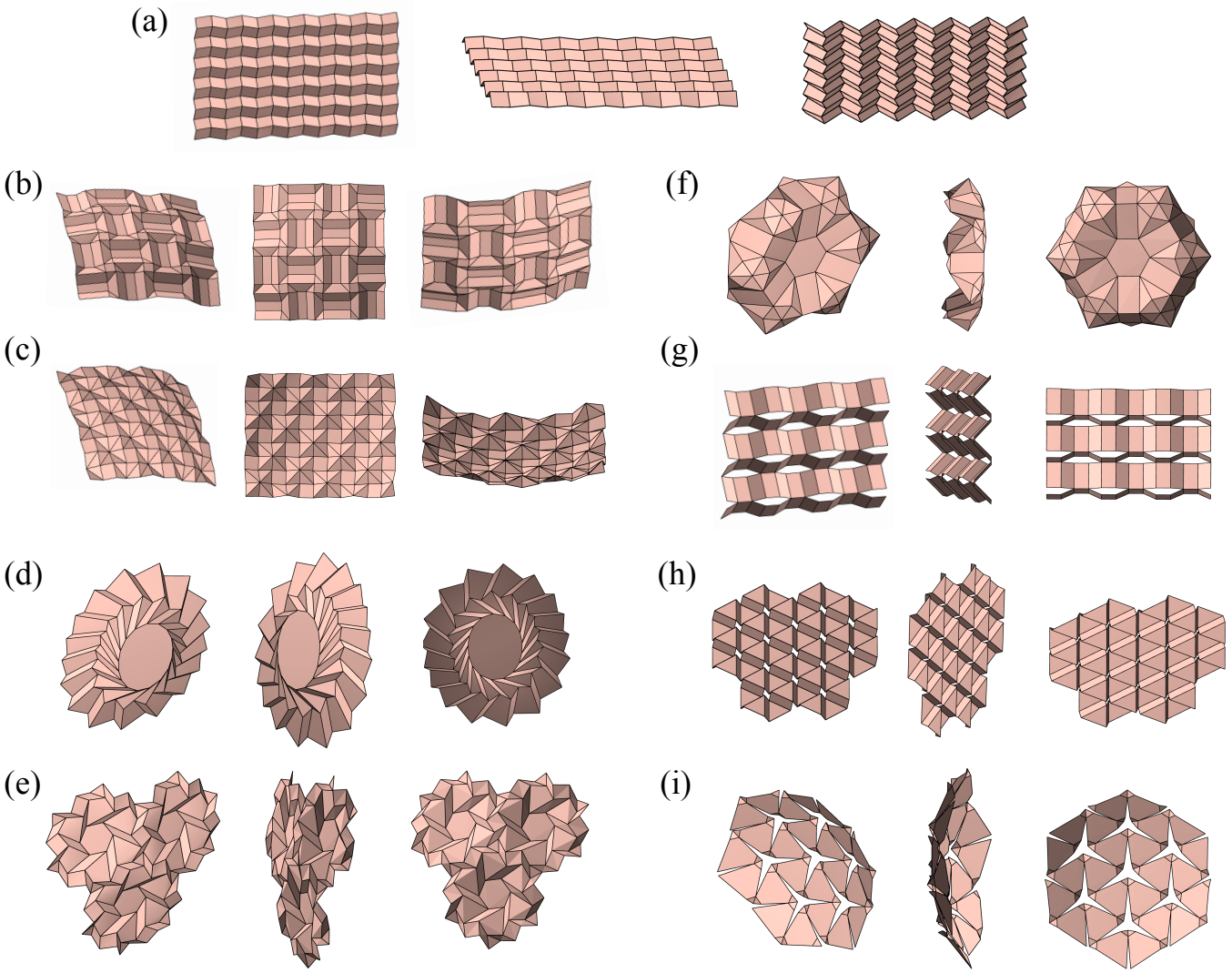

FIG. S1. **Different views of the nine types of origami structures considered in our study.** For each type, three different views are provided. (a) Miura-Ori. (b) Huffman Rectangular Weave. (c) Huffman Waterbombs. (d) Lang Oval. (e) Hex/Tri. (f) Lang Honeycomb. (g) Kirigami Honeycomb. (h) Perforated Triangle. (i) Auxetic Triangle.

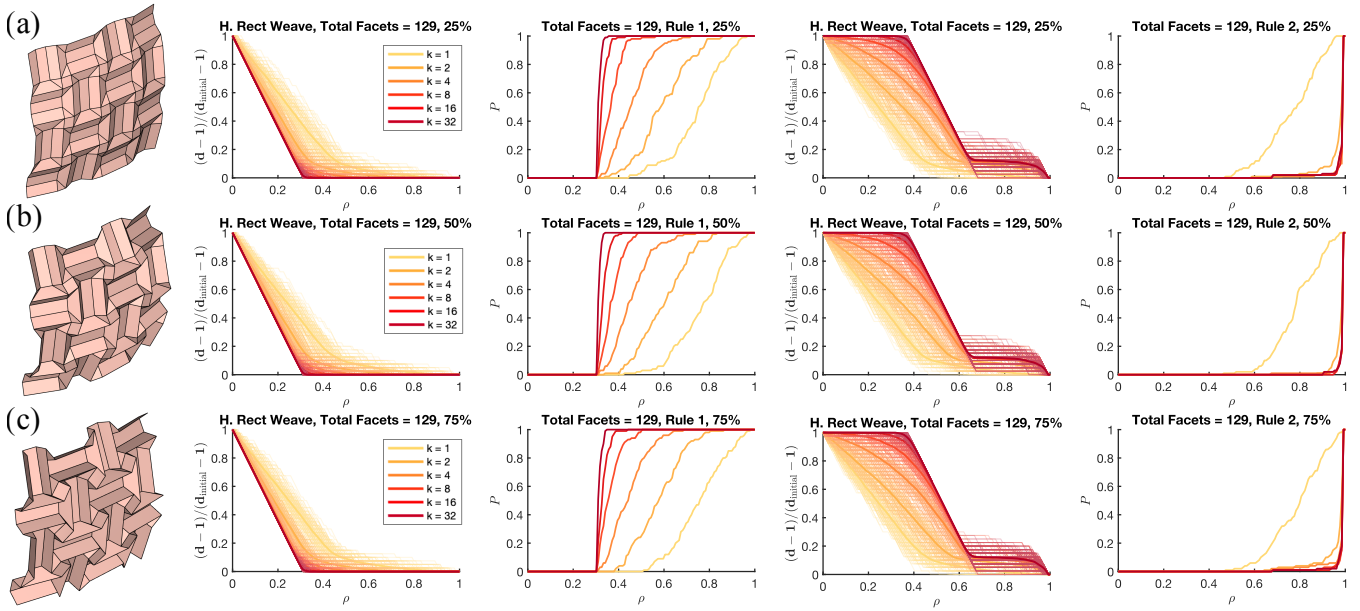

FIG. S2. **Comparing the explosive rigidity percolation in the Huffman Rectangular Weave Origami structure with different folding percentage θ.** (a) The results for $\theta = 25\%$. (b) The results for $\theta = 50\%$. (c) The results $\theta = 75\%$. For each folding percentage, we consider the Huffman Rectangular Weave Origami structure (left), the rigidity percolation simulation result based on the Most Efficient selection rule with different number of choices k, and the simulation result based on the Least Efficient selection rule (right). Here, ρ is the density of the planarity constraints explicitly imposed, and P is the probability of getting a final DOF structure.

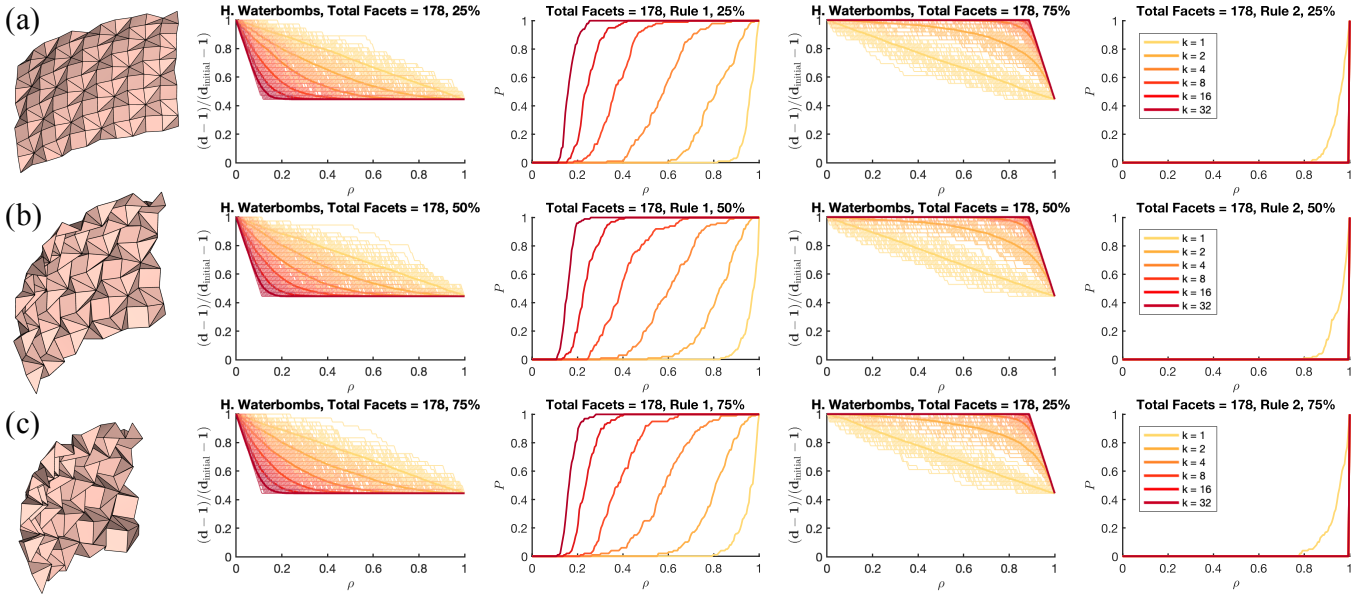

FIG. S3. **Comparing the explosive rigidity percolation in the Huffman Waterbombs Origami structure with different folding percentage θ.** (a) The results for $\theta = 25\%$. (b) The results for $\theta = 50\%$. (c) The results $\theta = 75\%$. For each folding percentage, we consider the Huffman Waterbombs Origami structure (left), the rigidity percolation simulation result based on the Most Efficient selection rule with different number of choices k, and the simulation result based on the Least Efficient selection rule (right). Here, ρ is the density of the planarity constraints explicitly imposed, and P is the probability of getting a final DOF structure.

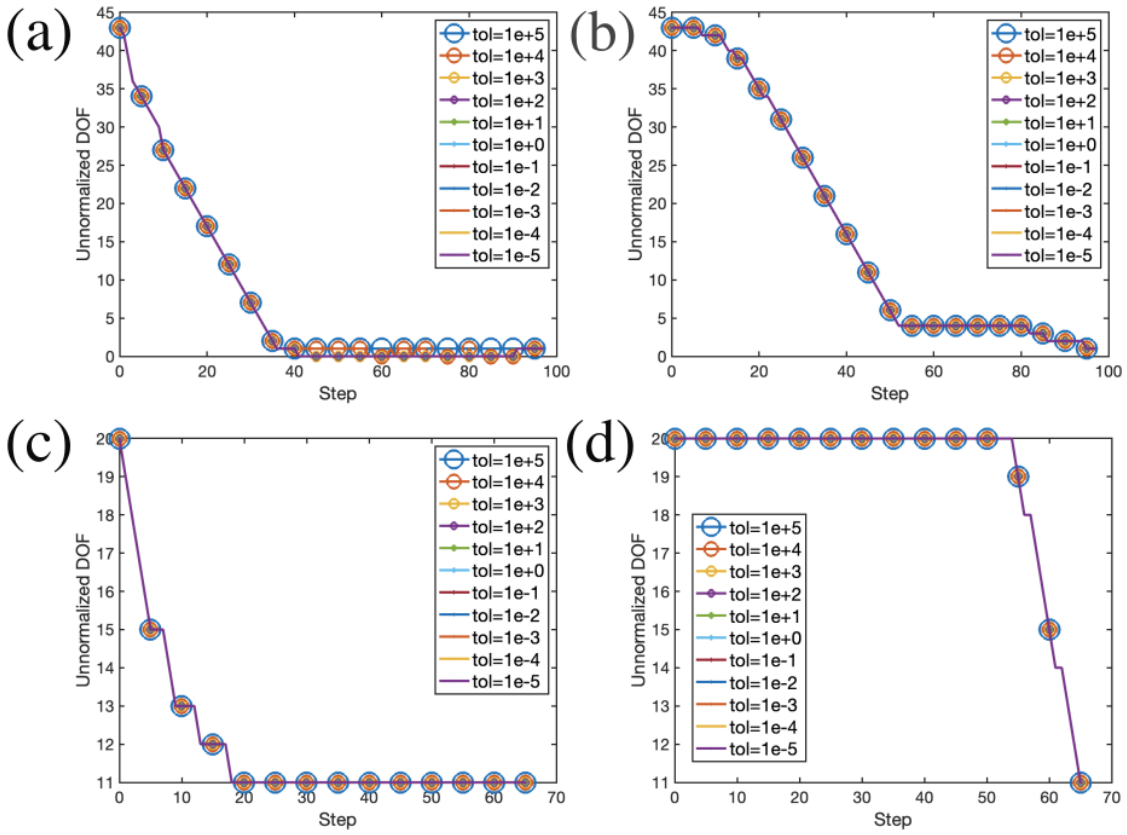

FIG. S4. **Sensitivity of the unnormalized DOF to the numerical-rank tolerance.** The plots show the unnormalized DOF trajectories over the selection steps under different tolerance multipliers in the numerical rank test. (a) Hex/Tri origami (Fig. 1 in the main text) with choice number $k = 16$ under the Most Efficient selection rule. (b) Hex/Tri origami (Fig. 1 in the main text) with choice number $k = 16$ under the Least Efficient selection rule. (c) Asymmetric origami (Fig. 2 in the main text) with choice number $k = 16$ under the Most Efficient selection rule. (d) Asymmetric origami (Fig. 2 in the main text) with choice number $k = 16$ under the Least Efficient selection rule.

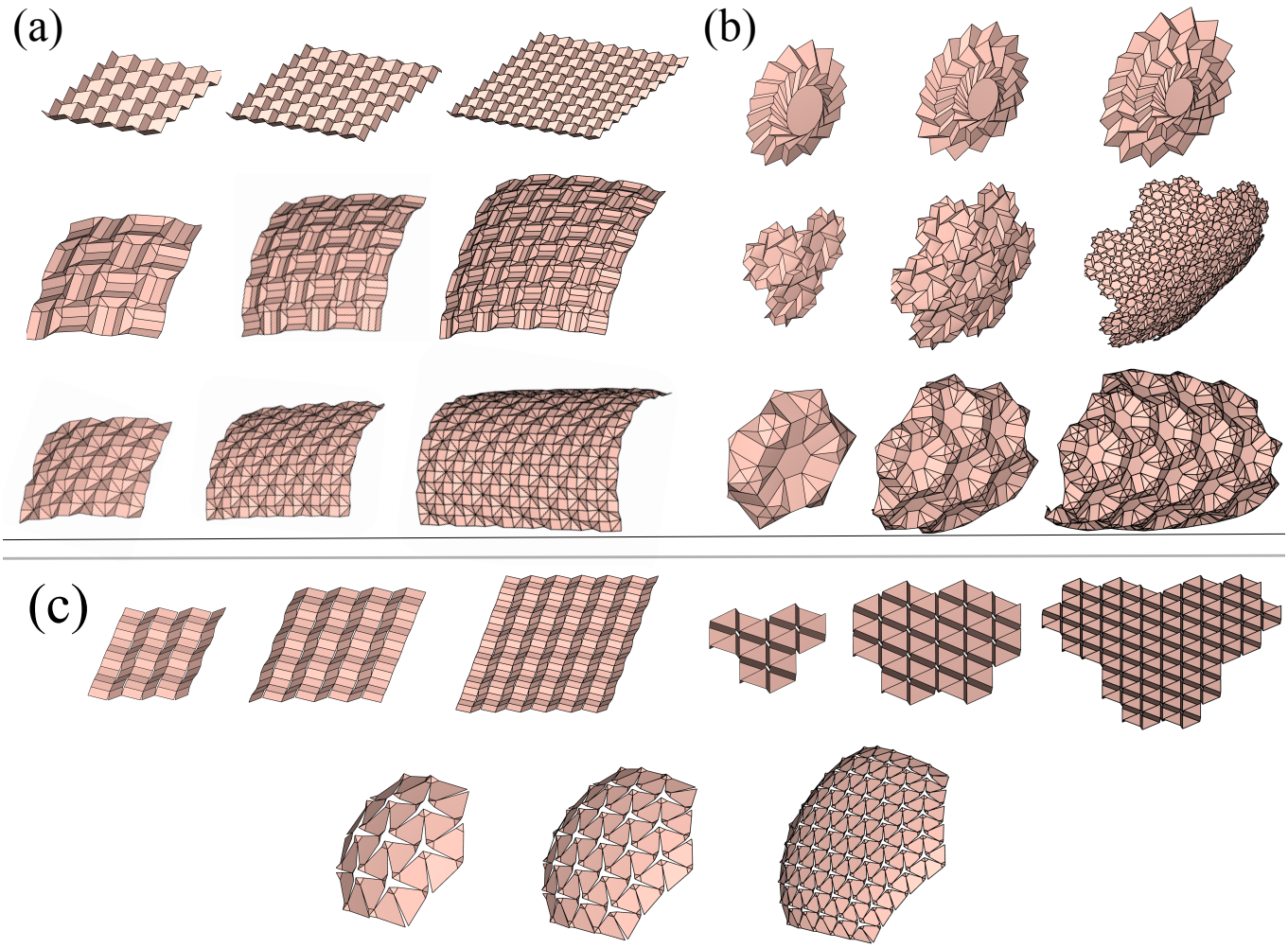

FIG. S5. **Nine types of origami structures with different resolutions considered in our additional analysis.** For each type of structure, three different resolutions are considered. (a) Periodic origami structures: Miura-ori (with 100, 225, and 400 facets), Huffman Rectangular Weave (with 129, 313, and 577 facets), and Huffman Waterbombs (with 178, 403, and 718 facets). (b) Rotational origami structures: Lang Oval (with 69, 103, and 137 facets), Hex/Tri (with 97, 205, and 1285 facets), and Lang Honeycomb (with 91, 367, and 829 facets). (c) Perforated origami structures: Kirigami Honeycomb (with 72, 120, and 276 facets), Perforated Triangle (with 39, 106, and 342 facets), and Auxetic Triangle (with 88, 206, and 570 facets).

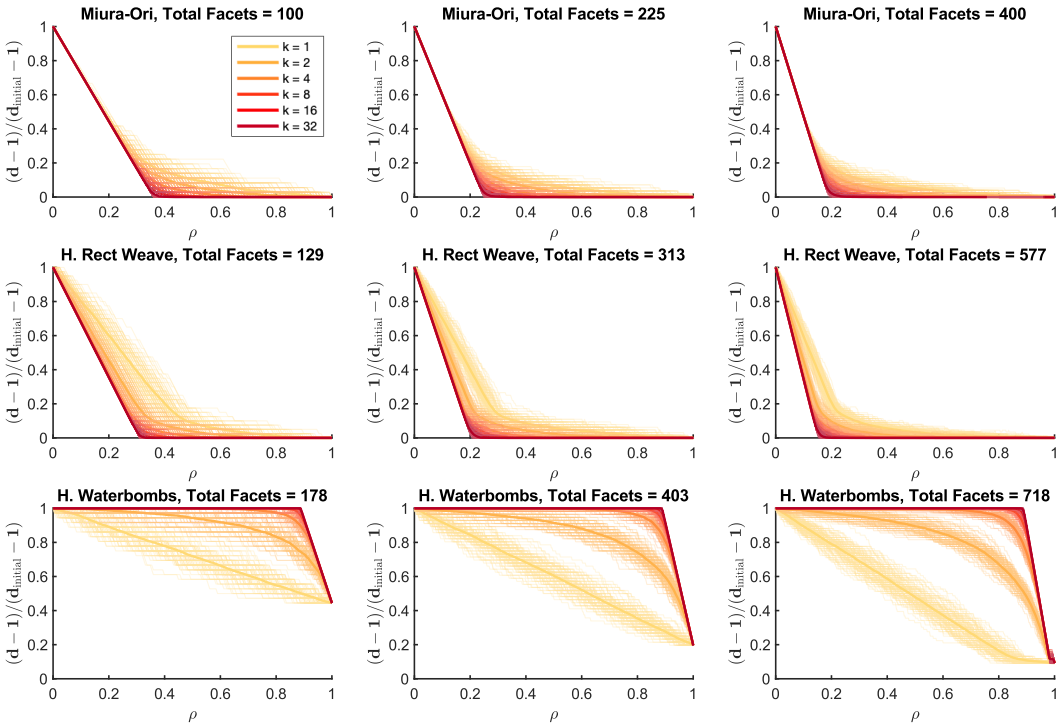

FIG. S6. **Change in the normalized DOF under the Most Efficient selection rule for three types of periodic origami structures with different sizes.** For each type and each size, different numbers of choices $k = 1, 2, 4, 8, 16, 32$ are considered.

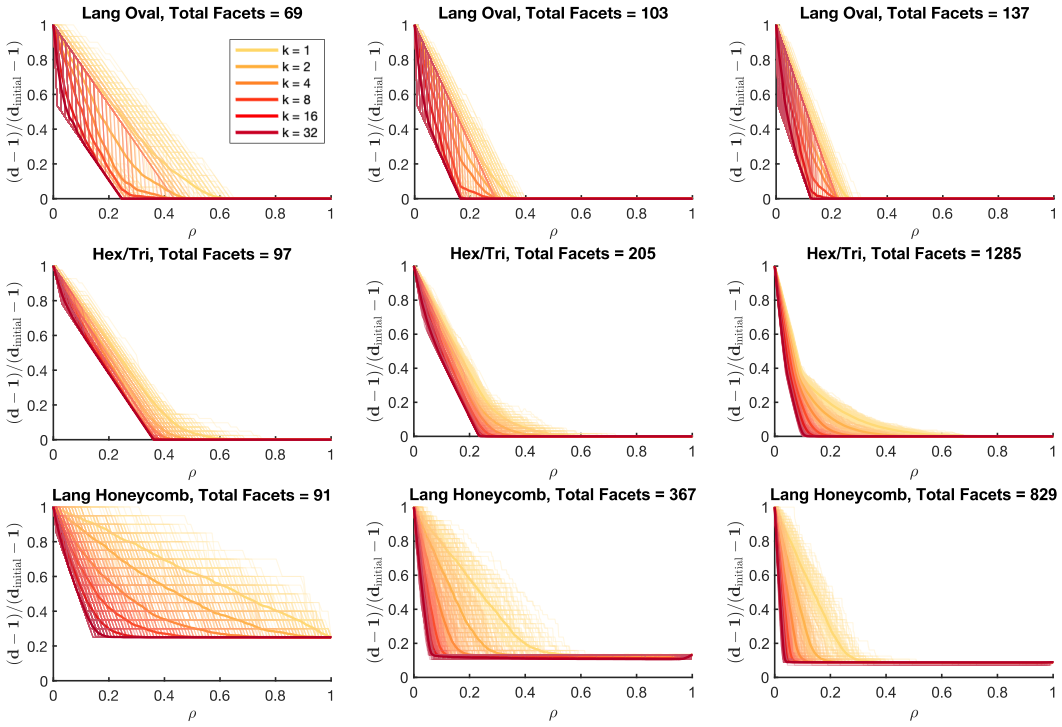

FIG. S7. **Change in the normalized DOF under the Most Efficient selection rule for three types of rotational origami structures with different sizes.** For each type and each size, different numbers of choices $k = 1, 2, 4, 8, 16, 32$ are considered.

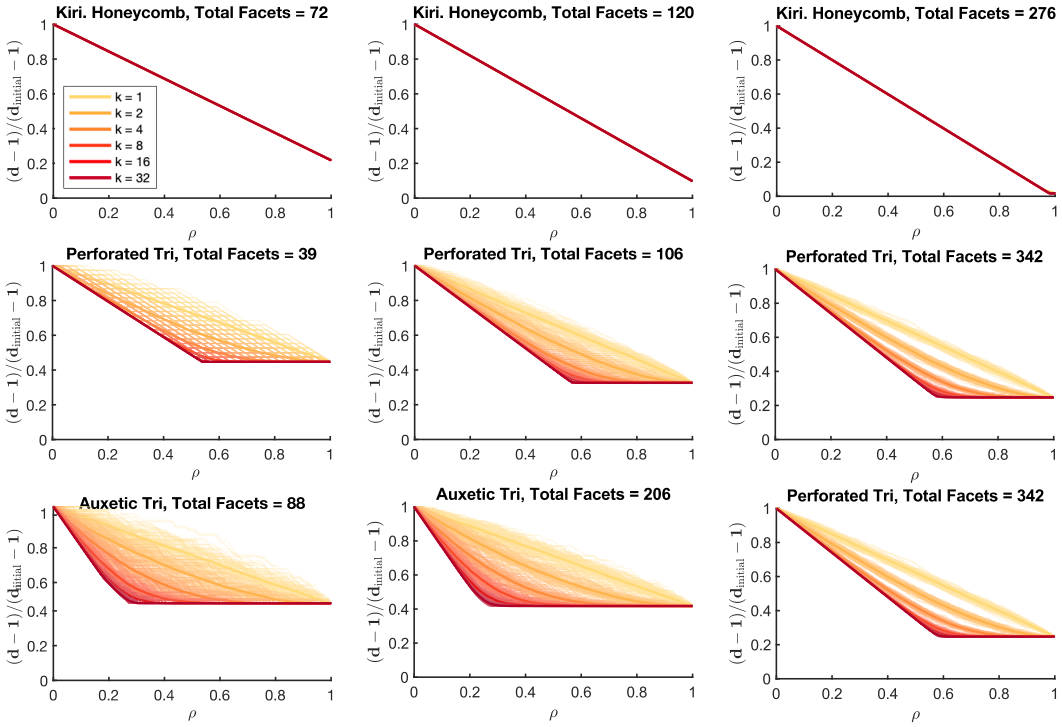

FIG. S8. **Change in the normalized DOF under the Most Efficient selection rule for three types of perforated origami structures with different sizes.** For each type and each size, different numbers of choices $k = 1, 2, 4, 8, 16, 32$ are considered.

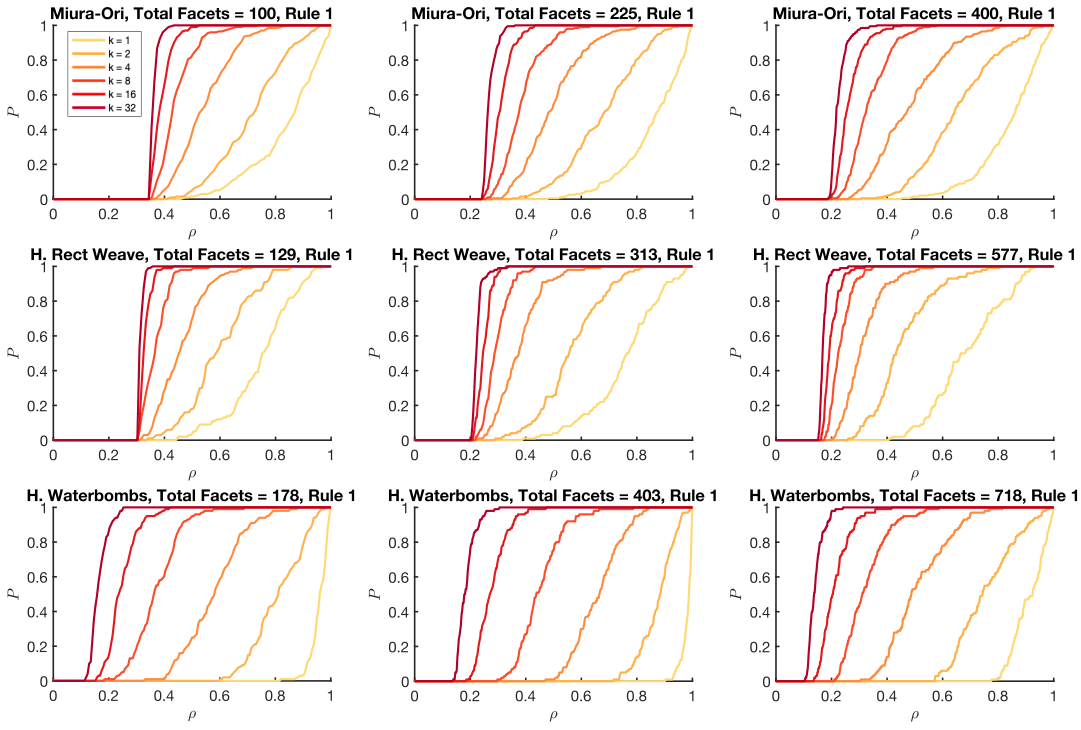

FIG. S9. **Rigidity percolation in periodic origami under the Most Efficient selection rule for three origami structures with different sizes.** For different problem sizes (with the total number of facets indicated in each subfigure title) and different numbers of choices $k = 1, 2, 4, 8, 16, 32$, we compute the probability P of obtaining a minimum-DOF structure at different planarity constraint densities ρ, based on 100 simulations.

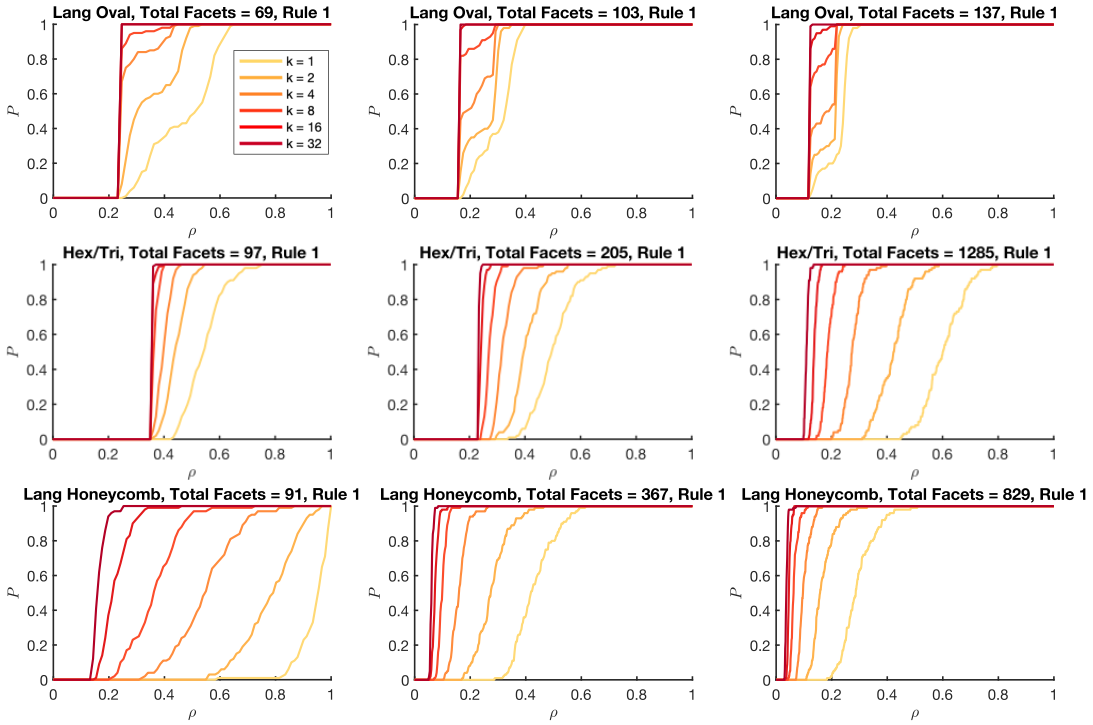

FIG. S10. **Rigidity percolation in rotational origami under the Most Efficient selection rule for three origami structures with different sizes.** For different problem sizes (with the total number of facets indicated in each subfigure title) and different numbers of choices $k = 1, 2, 4, 8, 16, 32$, we compute the probability P of obtaining a minimum-DOF structure at different planarity constraint densities ρ, based on 100 simulations.

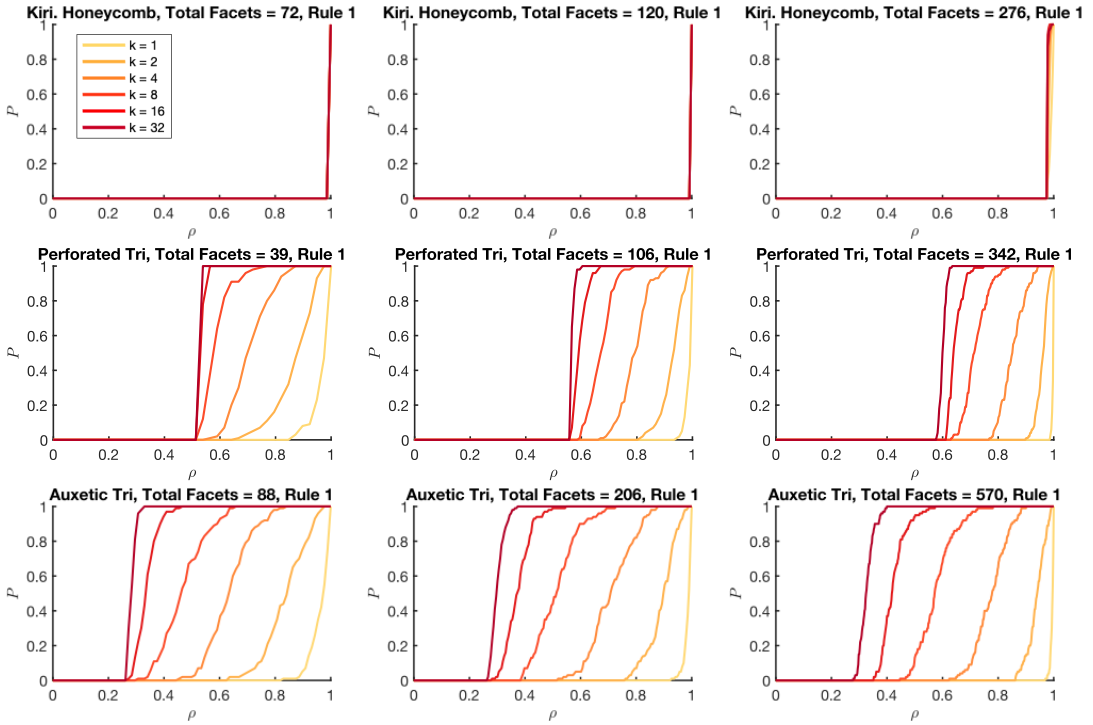

FIG. S11. **Rigidity percolation in perforated origami under the Most Efficient selection rule for three origami structures with different sizes.** For different problem sizes (with the total number of facets indicated in each subfigure title) and different numbers of choices $k = 1, 2, 4, 8, 16, 32$, we compute the probability P of obtaining a minimum-DOF structure at different planarity constraint densities ρ, based on 100 simulations.

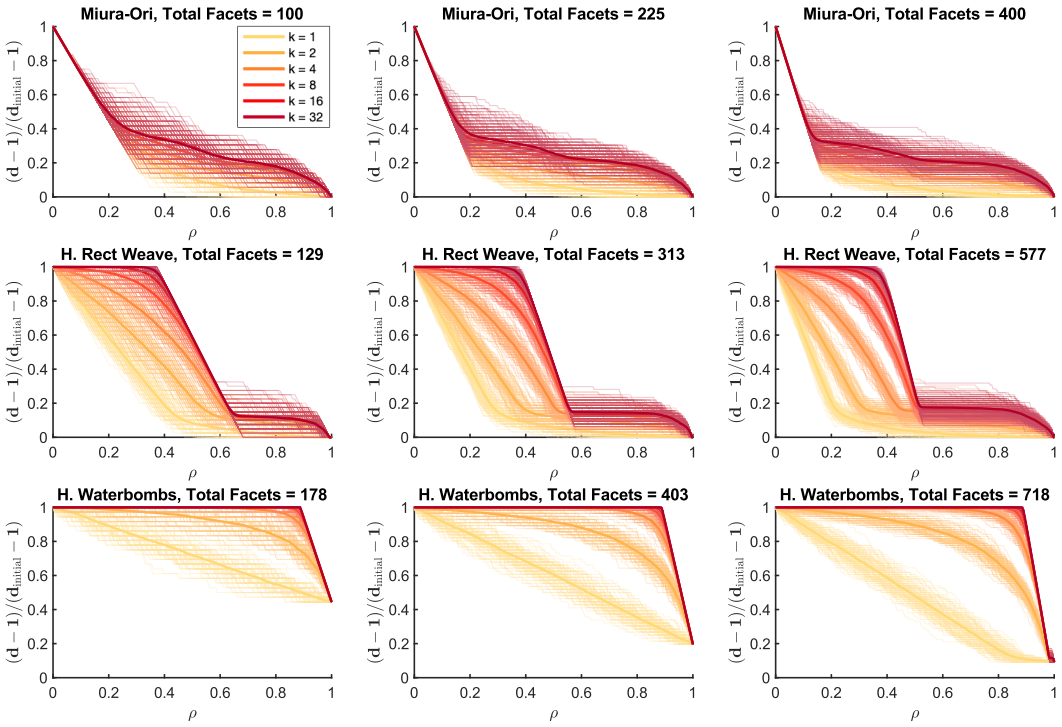

FIG. S12. **Change in the normalized DOF under the Least Efficient selection rule with different numbers of choices for three types of periodic origami structures with different sizes.** For each type and each size, different numbers of choices $k = 1, 2, 4, 8, 16, 32$ are considered.

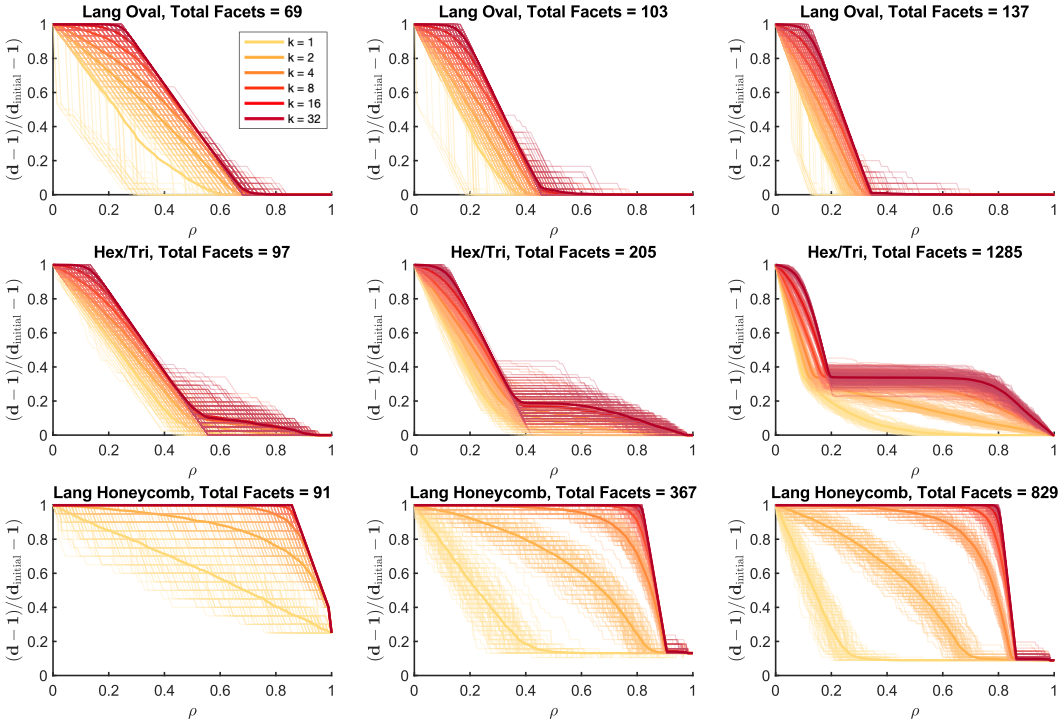

FIG. S13. **Change in the normalized DOF under the Least Efficient selection rule with different numbers of choices for three types of rotational origami structures with different sizes.** For each type and each size, different numbers of choices $k = 1, 2, 4, 8, 16, 32$ are considered.

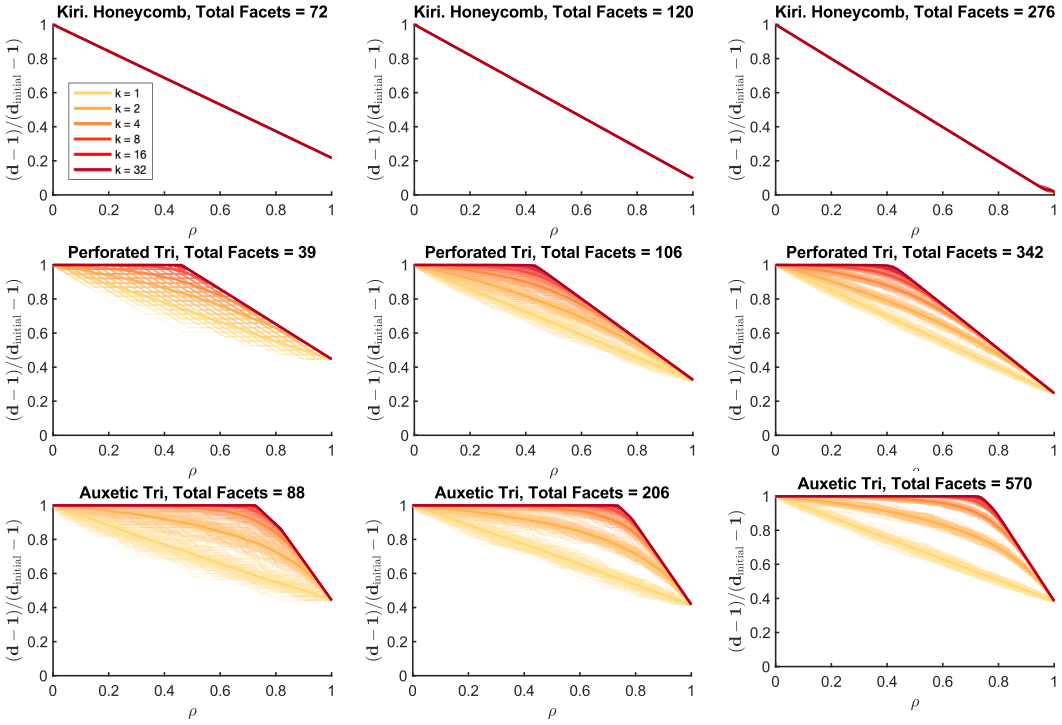

FIG. S14. **Change in the normalized DOF under the Least Efficient selection rule with different numbers of choices for three types of perforated origami structures with different sizes.** For each type and each size, different numbers of choices $k = 1, 2, 4, 8, 16, 32$ are considered.

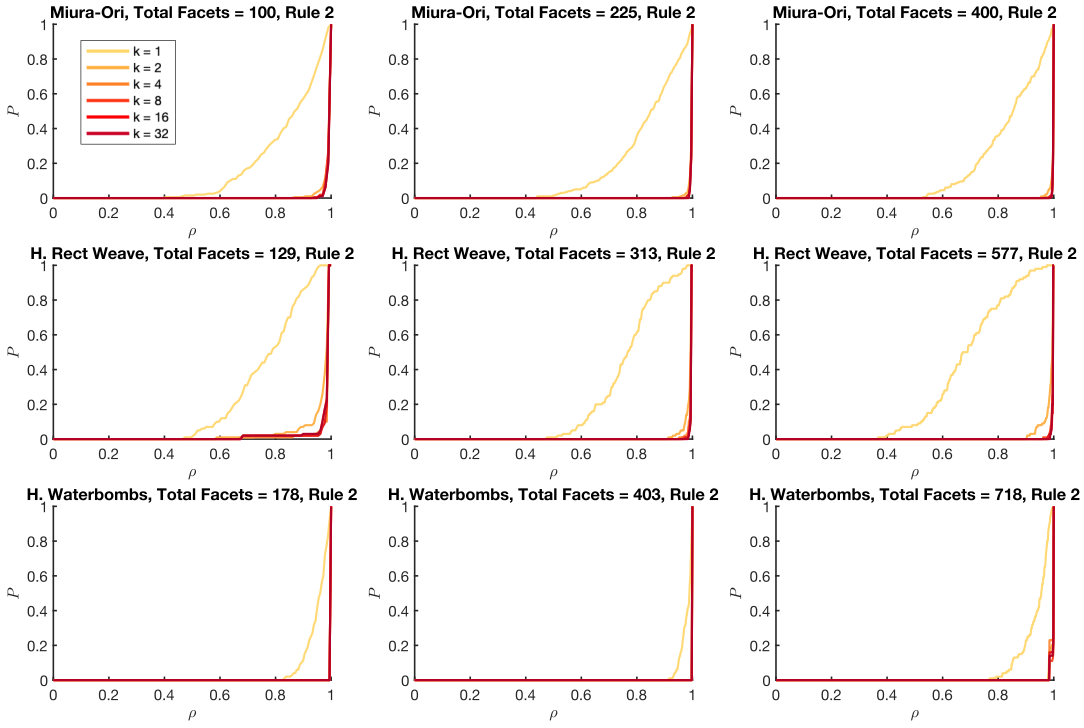

FIG. S15. **Rigidity percolation in periodic origami under the Least Efficient selection rule for three origami structures with different sizes.** For different problem sizes (with the total number of facets indicated in each subfigure title) and different numbers of choices $k = 1, 2, 4, 8, 16, 32$, we compute the probability P of obtaining a minimum-DOF structure at different planarity constraint densities ρ, based on 100 simulations.

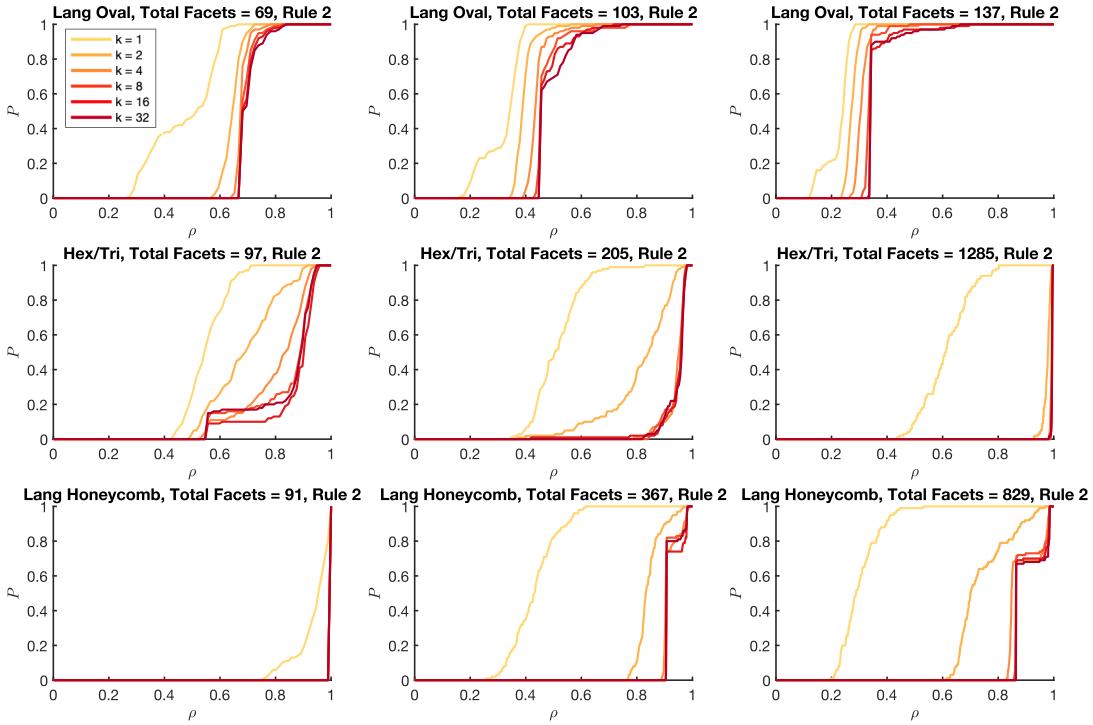

FIG. S16. **Rigidity percolation in rotational origami under the Least Efficient selection rule for three origami structures with different sizes.** For different problem sizes (with the total number of facets indicated in each subfigure title) and different numbers of choices $k = 1, 2, 4, 8, 16, 32$, we compute the probability P of obtaining a minimum-DOF structure at different planarity constraint densities ρ, based on 100 simulations.

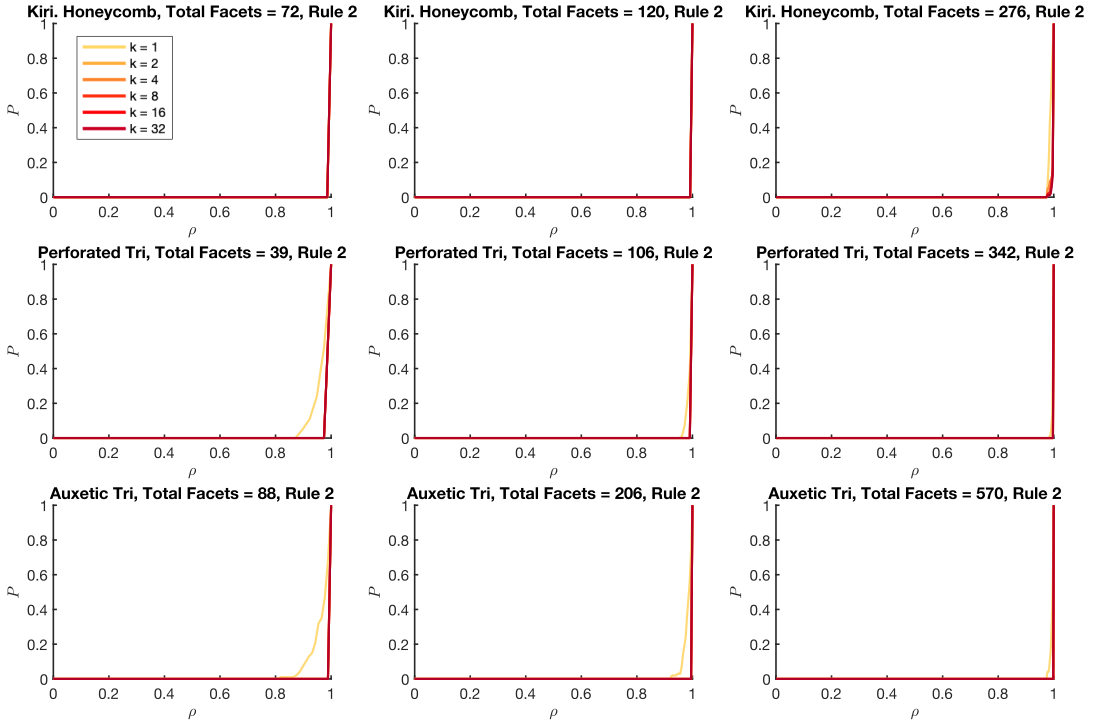

FIG. S17. **Rigidity percolation in perforated origami under the Least Efficient selection rule for three origami structures with different resolutions.** For different problem sizes (with the total number of facets indicated in each subfigure title) and different numbers of choices $k = 1, 2, 4, 8, 16, 32$, we compute the probability P of obtaining a minimum-DOF structure at different planarity constraint densities ρ, based on 100 simulations.

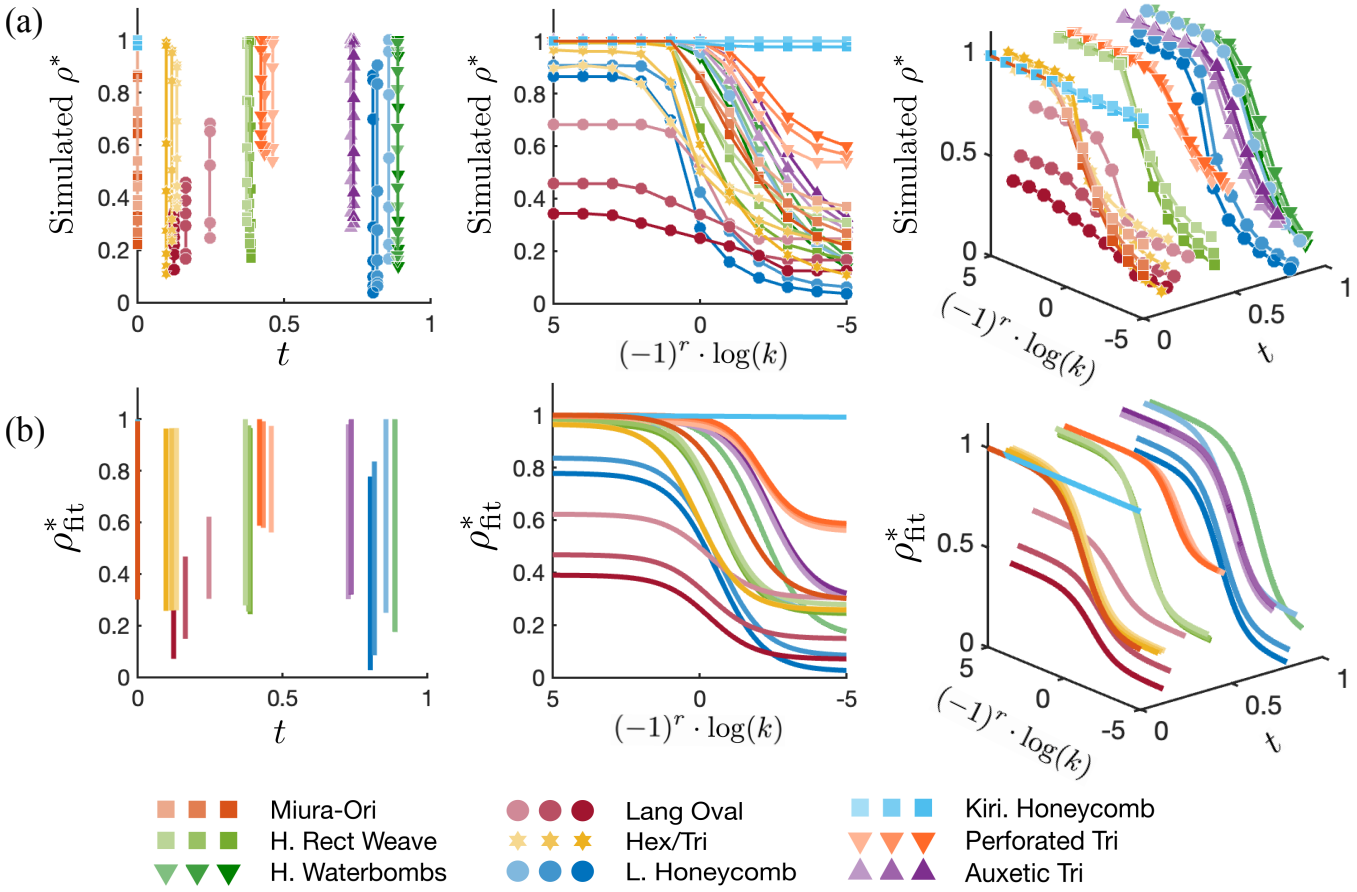

FIG. S18. **The simulated critical transition density ρ^* and the fitted values ρ^*_{fit} for the nine different types of origami structures under different selection rules and different number of choices k.** The nine different types of origami structures are represented using different color and marker styles. For each structure, three resolutions are considered, indicated by different marker transparencies (lower transparency corresponds to lower resolution; see the caption of Fig. S5 for detailed resolution information).(a) Simulated results: critical transition density ρ^* versus selection rule; ρ^* versus triangular facet ratio; and a 3D plot combining both variables. (b) Fitted results: fitted critical transition density ρ^*_{fit} versus selection rule; ρ^*_{fit} versus triangular facet ratio; and a 3D plot combining both variables.

Pattern Name	Number of Facets	Triangular Facet Ratio t	Number of Choices k	Most Efficient Selection Rule ρ^*	Least Efficient Selection Rule ρ^*
Miura-ori	100	0.00	1	0.8700	0.8700
			2	0.7300	1.0000
			4	0.6400	1.0000
			8	0.4400	1.0000
			16	0.3900	1.0000
			32	0.3700	1.0000
Miura-ori	225	0.00	1	0.8711	0.8533
			2	0.6844	1.0000
			4	0.4844	1.0000
			8	0.3822	1.0000
			16	0.3111	1.0000
			32	0.2667	1.0000
Miura-ori	400	0.00	1	0.8625	0.8550
			2	0.6450	1.0000
			4	0.4725	1.0000
			8	0.3275	1.0000
			16	0.2550	1.0000
			32	0.2200	1.0000
Huffman Rectangular Weave	129	0.37	1	0.7519	0.7909
			2	0.5891	0.9845
			4	0.4574	0.9922
			8	0.3721	0.9922
			16	0.3256	0.9922
			32	0.3101	0.9922
Huffman Rectangular Weave	313	0.38	1	0.7636	0.7688
			2	0.5559	0.9936
			4	0.3770	0.9968
			8	0.2875	0.9968
			16	0.2460	0.9968
			32	0.2236	0.9968
Huffman Rectangular Weave	577	0.39	1	0.6655	0.6724
			2	0.4333	0.9965
			4	0.3016	0.9983
			8	0.2236	0.9983
			16	0.1924	0.9983
			32	0.1681	0.9983
Huffman Waterbombs	178	0.89	1	0.9607	0.9607
			2	0.8146	1.0000
			4	0.5843	1.0000
			8	0.3652	1.0000
			16	0.2360	1.0000
			32	0.1629	1.0000
Huffman Waterbombs	403	0.89	1	0.9876	0.9901
			2	0.8834	1.0000
			4	0.6650	1.0000
			8	0.4392	1.0000
			16	0.2705	1.0000
			32	0.1787	1.0000
Huffman Waterbombs	718	0.89	1	0.9248	0.9554
			2	0.7437	1.0000
			4	0.4875	1.0000
			8	0.3106	1.0000
			16	0.2033	1.0000
			32	0.1379	1.0000

TABLE S1. **The critical transition density ρ^* for different periodic origami structures under the Most Efficient and Least Efficient selection rules with different number of choices k.**

Pattern Name	Number of Facets	Triangular Facet Ratio t	Number of Choices k	Most Efficient Selection Rule ρ^*	Least Efficient Selection Rule ρ^*
Lang Oval	69	0.25	1	0.5217	0.5217
			2	0.3043	0.6522
			4	0.2464	0.6812
			8	0.2464	0.6812
			16	0.2464	0.6812
			32	0.2464	0.6812
Lang Oval	103	0.17	1	0.3301	0.3495
			2	0.2913	0.3883
			4	0.1845	0.4369
			8	0.1650	0.4563
			16	0.1650	0.4563
			32	0.1650	0.4563
Lang Oval	137	0.17	1	0.2482	0.2482
			2	0.2190	0.2774
			4	0.1825	0.3066
			8	0.1241	0.3358
			16	0.1241	0.3431
			32	0.1241	0.3431
Hex/Tri	97	0.13	1	0.5464	0.5464
			2	0.4433	0.6907
			4	0.4021	0.8351
			8	0.3711	0.8966
			16	0.3608	0.9072
			32	0.3608	0.8969
Hex/Tri	205	0.12	1	0.4976	0.5073
			2	0.3951	0.8439
			4	0.3171	0.9512
			8	0.2732	0.9610
			16	0.2439	0.9610
			32	0.2341	0.9659
Hex/Tri	1285	0.10	1	0.6008	0.6086
			2	0.4233	0.9798
			4	0.2739	0.9922
			8	0.1852	0.9946
			16	0.1377	0.9946
			32	0.1097	0.9946
Lang Honeycomb	91	0.86	1	0.9560	0.9560
			2	0.7912	1.0000
			4	0.5495	1.0000
			8	0.3623	1.0000
			16	0.2198	1.0000
			32	0.1648	1.0000
Lang Honeycomb	367	0.82	1	0.4196	0.4305
			2	0.2752	0.8338
			4	0.1608	0.9046
			8	0.1008	0.9074
			16	0.0736	0.9074
			32	0.0627	0.9074
Lang Honeycomb	829	0.80	1	0.2871	0.2871
			2	0.1580	0.6996
			4	0.0965	0.8480
			8	0.0627	0.8649
			16	0.0458	0.8649
			32	0.0374	0.8649

TABLE S2. **The Critical transition density ρ^* of different rotational origami structures under the Most Efficient and Least Efficient selection rules with different number of choices k.**

Pattern Name	Number of Facets	Triangular Facet Ratio t	Number of Choices k	Most Efficient Selection Rule ρ^*	Least Efficient Selection Rule ρ^*
Kirigami Honeycomb	72	0.00	1	1.0000	1.0000
			2	1.0000	1.0000
			4	1.0000	1.0000
			8	1.0000	1.0000
			16	1.0000	1.0000
			32	1.0000	1.0000
Kirigami Honeycomb	120	0.00	1	1.0000	1.0000
			2	1.0000	1.0000
			4	1.0000	1.0000
			8	1.0000	1.0000
			16	1.0000	1.0000
			32	1.0000	1.0000
Kirigami Honeycomb	276	0.00	1	0.8711	0.4200
			2	1.0000	1.0000
			4	1.0000	1.0000
			8	1.0000	1.0000
			16	1.0000	1.0000
			32	1.0000	1.0000
Auxetic Triangle	88	0.73	1	0.9773	0.9886
			2	0.8523	1.0000
			4	0.6364	1.0000
			8	0.4659	1.0000
			16	0.3409	1.0000
			32	0.2814	1.0000
Auxetic Triangle	206	0.74	1	0.9903	0.9903
			2	0.8981	1.0000
			4	0.7089	1.0000
			8	0.5149	1.0000
			16	0.3738	1.0000
			32	0.3010	1.0000
Auxetic Triangle	570	0.74	1	0.9965	0.9965
			2	0.9404	1.0000
			4	0.7789	1.0000
			8	0.5719	1.0000
			16	0.4175	1.0000
			32	0.3246	1.0000
Perforated Triangle	49	0.46	1	1.0000	1.0000
			2	0.8974	1.0000
			4	0.7179	1.0000
			8	0.5897	1.0000
			16	0.5385	1.0000
			32	0.5385	1.0000
Perforated Triangle	106	0.43	1	1.0000	1.0000
			2	0.9340	1.0000
			4	0.7925	1.0000
			8	0.6698	1.0000
			16	0.5940	1.0000
			32	0.5560	1.0000
Perforated Triangle	225	0.00	1	1.0000	1.0000
			2	0.9620	1.0000
			4	0.8509	1.0000
			8	0.7135	1.0000
			16	0.6404	1.0000
			32	0.5994	1.0000

TABLE S3. **The critical transition density ρ^* of different perforated origami structures under the Most Efficient and Least Efficient selection rules with different number of choices k.**

Structure	**a**	**b**	**c**	**d**	**f**	**RMSE**	**Normalized RMSE**
Miura-Ori	0.353314	0.615089	0.766633	0.000000	0.647008	0.035586	7.74%
Huffman Rectangular Weave	0.361662	0.727425	0.475935	-2.124972	1.429219	0.047417	6.20%
Huffman Waterbombs	0.423211	0.617756	1.279683	-1.167508	1.613251	0.036420	4.82%
Lang Oval	0.160092	0.632491	0.212309	1.900514	-0.005942	0.051558	15.03%
Hex/Tri	0.354397	0.655452	-0.038231	0.048151	0.605736	0.072726	11.97%
Lang Honeycomb	0.377366	0.629517	0.382077	4.134894	-2.920914	0.104569	16.39%
Kirigami Honeycomb	2.132125	0.000368	0.115862	0.000000	0.750164	0.006987	0.69%
Perforated Triangle	0.208261	0.831877	1.741861	-0.650196	1.065508	0.025120	2.53%
Auxetic Triangle	0.349825	0.656863	1.559848	1.884478	-0.740271	0.026843	3.10%

TABLE S4. **The fitted model parameters, the root mean square error (RMSE), and the normalized RMSE** for each type of origami structure considered in this work.